Fuel 257 (2019) 116005

Contents lists available at ScienceDirect

Fuel

journal homepage: www.elsevier.com/locate/fuel

Full Length Article

The effects of mineral distribution, pore geometry, and pore density on permeability evolution in gas shales

B. Schwartz[a,*], K. Huffman[b], D. Thornton[c], D. Elsworth[a]

[a] G3 Center, The Pennsylvania State University, University Park, USA
[b] Chevron Mid-continent Business Unit, Midland, USA
[c] Chevron Energy Technology Company, Houston, USA

ARTICLE INFO

Keywords:
Shale permeability
Mineral distribution
Pore geometry
Gas shale

ABSTRACT

We explored the ensemble effects of pore density, pore geometry, and pore stiffness on the permeability evolution of an ellipsoidal pore under both applied uniaxial stress and relative pore pressure change. We found that rocks undergoing identical compressional strain and pore pressure can undergo significantly different magnitudes of pore closure or dilation based on the concomitant influence of these three variables. This is especially important in gas shales, where nano-porosity is challenging to characterize and heterogeneity at all scales has led to disparate permeability responses in both the field and laboratory. Simulations were carried out using a finite element solver, a method that allowed each variable to be studied in isolation and concomitantly. We found that the aspect ratio is the most sensitive parameter influencing pore compressibility. The pore density becomes important when external stress is applied, but it has no significant effect when pore pressure is varied in the absence of external stress. To capture the effects of mineral precipitation and transformation in pore walls, we simulated mismatches between the mineral stiffness of the pore and the surrounding matrix. We determined that for a given strain, mineralogically soft pores (soft relative to the bulk material) experience higher increase in permeability than pores that are mineralogically stiff relative to the surrounding matrix. While soft pores experience greater closure than stiff pores for a given applied stress, they also experience a greater amount of dilation when pore pressure increases.

1. Introduction

Shales are tight sedimentary rocks that consist—among other components—of organic matter, quartz cement and silt, carbonates, pyrite, feldspar and various clays including illite and smectite. The highly heterogenous nature of shale has made its response to changes in effective stress challenging to predict in both the lab and in the field. Due to variations in depositional environment, mineralogy, burial history and thermal maturation the internal pore structure of shale is complex. Pore channels in shale are nanometer to micrometer wide fractures separated by finely laminated stacks of minerals [1,2]. Permeability measurements of the intact rock range from 10^{-23} m^2 to 10^{-17} m^2 [3]. Within the matrix, there are two distinct planes for flow oriented orthogonal to bedding—the flow paths in the bedding-perpendicular direction are often typified as highly tortuous nano-sized capillary tubes [4–6], whereas the flow paths in the bedding-parallel direction can be modeled as long penny-shaped cracks [7,8]. This study focuses on the latter and considers Darcian flow in the bedding parallel direction through large pores found between bedding planes in the matrix. As these pores are much larger than those found in the bedding-perpendicular direction, Darcian flow models developed for larger fracture systems will capture the meaningful transport response under evolving stresses. Therefore, the results presented here are relevant for matrix permeability as well as induced fracture permeability in shales.

Pore channels in rocks are located near grain boundaries. The potential mismatch in material properties of the minerals surrounding a pore often leads to microcrack growth [9]. It can also create an environment in which the material properties of the pore boundary are different than the surrounding matrix. The mineral constituents of shale each have their own material properties, and the combination of mineralogy, grain orientation, and pore structure determine the bulk mechanical and transport properties of the intact shale. For organic-rich shales, pore channels residing within the organic matter are considered a substantial portion of the entire pore structure [10]. In addition to the organic matter, the clay portion of shales holds much of the remaining pore structure [11,12]. Indeed, some shales such as the Marcellus and

* Corresponding author at: 105 Hosler Building, University Park 16802, USA.
E-mail address: schwartz@psu.edu (B. Schwartz).

https://doi.org/10.1016/j.fuel.2019.116005
Received 26 June 2019; Received in revised form 8 August 2019; Accepted 9 August 2019

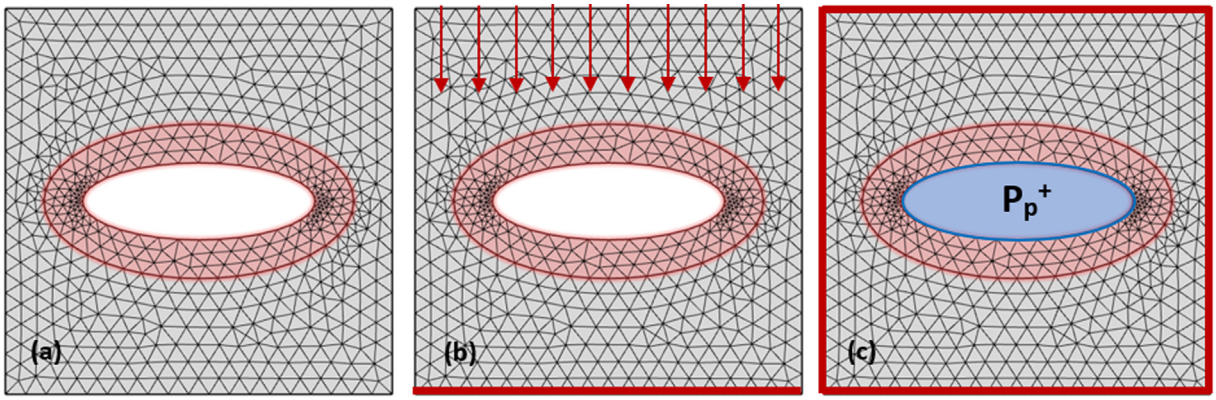

Fig. 1. (a) shows the schematic of each square in COMSOL. Two configurations were tested. The first was uniaxial strain applied to the top face of the square and is pictured in (b). The second was incremental increases in pore pressure with zero displacement along all exterior boundaries and is pictured in (c).

Utica shales are predominantly composed of clays and organic matter. Other shales such as the Wolfcamp have been found to be composed of much higher amounts of quartz and carbonates, suggesting that the pores may be located in stiffer materials than in organic-rich and clay-rich basins. In contrast to clays and organic matter, minerals such as quartz, feldspars, and carbonates have rigid grains that resist mechanical compaction [13]. Data have been collected on the stiffness of different minerals that comprise shale and vary over approximately one order of magnitude [14]. Exploring the permeability evolution of such pores with varying mineral distribution is the goal of this study.

In addition to the mineral composition of its boundary, pore compressibility is determined by its geometry. Flow paths in shales can be described as circular tubes, ellipsoidal pores, or flat cracks [15–17]. The main parameter used to differentiate between these geometries is the aspect ratio α of an ellipse where b is the semi-minor axis half length, a is the semi-major axis half length, and α is b/a. An α value of unity is a circle, and as α becomes much smaller than unity it transitions from describing an ellipse to describing a flat crack. Pore compressibility and pores density can be cast in terms of the perimeter and initial area of the ellipse, where the perimeter must be approximated and the area is πab [18,19]. Two-dimensional imaging has found that pore channels in the organic portion of shale vary from nearly round patches where α is between 0.5 and 1.0 to thin layers where α is less than 0.05 [20]. For example, the optimum value of α in the Bakken shale to match field data is 0.10 [21,22]. Disparities in average values of α within a basin are important, as the closing pressure for a penny shaped crack is directly proportional to its aspect ratio [23]. The compressibility of two-dimensional pores can be modeled analytically [24–26]. The only geometry suitable to analytical modeling in three dimensions is the penny shaped crack, which was found to be stiffer than the two-dimensional equivalent by a factor of $\pi/2$ [27]. In this study we will rely on two-dimensional modeling of pore compressibility: the axisymmetric nature of shale causes the three-dimensional case to reduce to the two-dimensional case when flow is studied parallel to the dominant pore network found in the bedding-parallel direction.

The third variable that affects permeability evolution in shale is the pore density b/s, where s is the spacing between fractures and b is the fracture aperture. When pores are soft compared to the surrounding matrix, the change in pore aperture Δb can be approximated as the product $s\varepsilon$, where ε is the bulk external strain [28]. Large values of s or ε will cause large changes in aperture. The ability to flow fluid through a fracture set is predominantly a function of the fracture aperture, and gas production is typically modelled as flow between parallel plates [29]. Fracture spacing is known to be related to bedding thickness and the degree of rock compaction during burial [30–32]. Spacing is often proportional to fracture aperture [33]. While it will vary spatially, the spacing determined by permeability measurements will reflect an average [34,35]. In the case of fracture sets of various sizes and roughness, the calculated aperture will be an average aperture over the entire fracture set [36,37]. In a one-dimensional case with a single fracture set pore density (b/s) is identical to porosity. The inverse (s/b) is called the spacing to aperture ratio and is often used to solve the cubic law—"spacing" is referring to the average distance between pores. Moving to the two-dimensional and three-dimensional cases, b/s is still indicative of pore density and porosity, just not in the exact sense as the one-dimensional case. They change by factors of 2 and 3, respectively (1b/s, 2b/s and 3b/s if apertures and spacing are the same in 3 orthogonal directions). However, the term b/s is still very useful in 2D and 3D, as a low b/s will correspond to a low porosity and vice versa – these factors change by orders of magnitude so a factor of 1–3 is inconsequential. One of the main goals of this paper is to show that b/s is an exceptionally powerful index in understanding how different pore densities accommodate deformation and permeability evolution.

Mineral distribution around pores, pore geometry, and pore spacing should all influence permeability evolution in shales. Anisotropy influenced by these variables have been measured in the laboratory [38–41], via optical imaging techniques [10,42–44], capillary pressure techniques [45], NMR [46–48], and digital core techniques [49–51]. In the work of Schwartz et al. (2019), laboratory studies showed that under the same effective stress, the permeability of shales evolve differently [52]. The goal of this study is to explore the contributions of each of the above three variables to the response of a shale undergoing changes in effective stress. To that end, we created a two-dimensional simulation of a pore that captures changes in mineral stiffness, pore geometry, and pore spacing. We tested two configurations: uniaxial strain and varying pore pressure. Next, we describe the study parameters.

2. Model description

We used COMSOL Multiphysics to model 2D stress evolution in square prismatic samples containing a central pore channel. The 3D case essentially reduces to the 2D case. Fig. 1a shows a schematic of the model geometry. A square with side length s was created and an ellipse with aspect ratio 1/3 was removed from the center. A second ellipse was created and is shown in Fig. 1 as a red band surrounding the pore space. This band was given a different material stiffness than the surrounding matrix pictured in grey in Fig. 1. The matrix stiffness K_m was set constant at 10 GPa. Assigning the "skeletal stiffness" of the red band as K_{sk} and the matrix stiffness as K_m, we were able to create a dimensionless ratio K_{sk}/K_m in order to capture changes in aperture Δb at constant spacing and external stress while varying K_{sk}/K_m. We varied K_{sk}/K_m from 10^{-3} to 10^{3} as this range is sufficient to capture mismatches between clays, quartz, calcite, pyrite, organic matter, and other common constituents of shale. We built prismatic blocks with side lengths s increasing from 5 to 10^4. Fig. 1b illustrates the first

configuration in which uniaxial stress was applied normal to the semi-major axis of the ellipse with the bottom face of the square fixed in space. Stress was varied such that it created a bulk strain that varied between 0 and $3.5e^{-3}$. The right and left sides of the square were allowed to deform freely. The result was a deformed square with a partially closed pore channel. At each stress, the change in ellipse aperture Δb was measured. In the second configuration, illustrated in Fig. 1c, all four exterior boundaries were fixed in space and pore pressure was applied as a traction normal to the boundary of the pore. Pore pressure was varied between 0 and 100 MPa. For both configurations, the only aspect ratio modeled in COMSOL was 1/3. We applied an analytical solution to incorporate changing aspect ratio into the model results.

3. Theory

3.1. Aspect ratio

Pore compressibility can be cast as

$$C_{pc} = \frac{2(1-\nu_m)}{G_m}\left(\alpha + \frac{1}{\alpha}\right) \tag{1}$$

where ν_m and G_m are the Poisson ratio and shear modulus of the intact rock, respectively [27]. As α becomes much smaller than unity, the equation can be simplified as

$$C_{pc} = \frac{2(1-\nu_m)}{G_m \alpha} \tag{2}$$

We plot Eq. (1) below to show pore compressibility as it varies with aspect ratio. We assume an intact Poisson ratio of 0.20 and shear modulus ranging from 1 to 1000 GPa. For α between 0.20 and 1.0, the pore compressibility is roughly constant. At α less than 0.20, the pore compressibility begins to increase dramatically, suggesting that shales with aspect ratios lower than 0.20 will experience significantly greater pore closure for a given compressive strain than shales with aspect ratios higher than 0.20.

3.1.1. Fixed aspect ratio

Strain in the pore space is defined as

$$\varepsilon_{pc} = \sigma' C_{pc} \tag{3}$$

We invoke the constraint that under hydrostatic stress the aspect ratio α can be assumed constant—a change in one semi-axis should be met by the same change in the other semi-axis due to equal stresses in all directions. Mathematically, this is

$$\frac{b}{a} = const. \rightarrow \frac{b(1-\frac{\Delta b}{b})}{a(1-\frac{\Delta a}{a})} = \frac{b}{a} \tag{4}$$

Assume that an ellipse with area A deforms into a new area A_2. Then

$$\frac{A_2}{A} = 1 - \frac{\Delta A}{A} = \left(1-\frac{\Delta a}{a}\right)\left(1-\frac{\Delta b}{b}\right) \tag{5}$$

We note that the quantities in parenthesis should be equal under the constraint of Eq. (4). The two-dimensional strain in the pore space can therefore be recast as

$$\varepsilon_{pc} = \frac{\Delta A}{A} \rightarrow \varepsilon_{pc} = 1 - \left(1-\frac{\Delta b}{b}\right)^2 \tag{6}$$

Combining (3) and (6) we have

$$\varepsilon_{pc} = \Delta\sigma' C_{pc} = 1 - \left(1-\frac{\Delta b}{b}\right)^2 \tag{7}$$

Since fluid flow in shale can be modeled as flow between parallel plates [29],

$$\frac{k}{k_o} = \left(1-\frac{\Delta b}{b_0}\right)^3 \tag{8}$$

Eq. (7) can be recast as

$$\frac{k}{k_0} = (1-\Delta\sigma' C_{pc})^{\frac{3}{2}} \tag{9}$$

3.1.2. Changing aspect ratio

In the case that the aspect ratio is not held constant, Δα can be modeled as occurring only along the minor semi-axis: aperture closure. In that case, the change in area of the ellipse is

$$\Delta A = \pi ab\left(1-\frac{\Delta b}{b}\right) \tag{10}$$

and the pore strain becomes

$$\varepsilon_{pc} = \frac{\pi ab - \pi ab(1-\frac{\Delta b}{b})}{\pi ab} = 1 - \left(1-\frac{\Delta b}{b}\right) \tag{11}$$

It can be readily shown that Eq. (9) becomes

$$\frac{k}{k_0} = (1-\Delta\sigma' C_{pc})^3 \tag{12}$$

in the case of changing aspect ratio due to a change in aperture *b*.

We normalize the permeability in Eqs. (9) and (12) to an aspect ratio α of 1/3 in order to match the remainder of the simulation. Fig. 3 shows the change in permeability as α decreases under constant stress. At aspect ratios greater than 0.20, permeability loss is small. However, as α continues to decrease and pore compressibility continues to increase, the permeability loss becomes much larger. This is in agreement with Fig. 2, which shows that the main driver of the additional permeability loss at constant external stress is the pore compressibility. It can be seen from Fig. 3 that, if the only difference between two shales is that one has an average aspect ratio of 0.20 and the other an aspect ratio of 0.02, the permeability loss at constant effective stress goes from 0.98 to 0.50.

In both scenarios, the curves reach the lower bound of k/k_0 as α approaches 10^{-2}. Examining Eqs. (9) and (12) shows that this occurs when $\sigma' C_{pc}$ becomes greater than 1. As the applied effective stress is 10^7 Pa, the lower bound is reached when C_{pc} is $10^{-7}\,Pa^{-1}$. This is a mathematical constraint to the equations, and all values of α that take C_{pc} higher than this physical limit should be interpreted as causing complete pore closure.

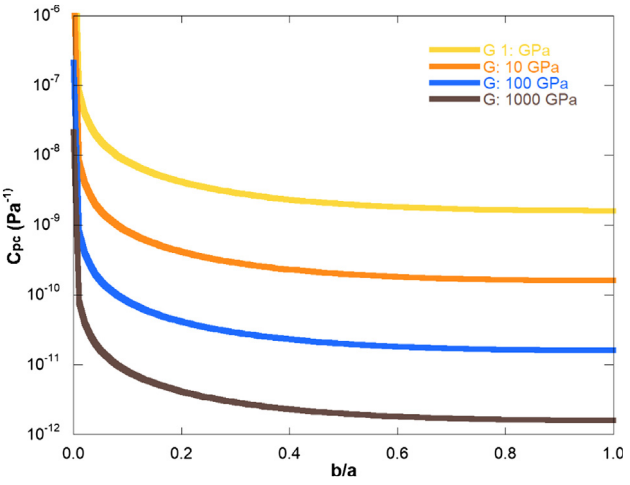

Fig. 2. Pore compressibility vs aspect ratio shows that pore compliance increases by an order of magnitude once α becomes less than 0.20, an aspect ratio b/a of 0.2.

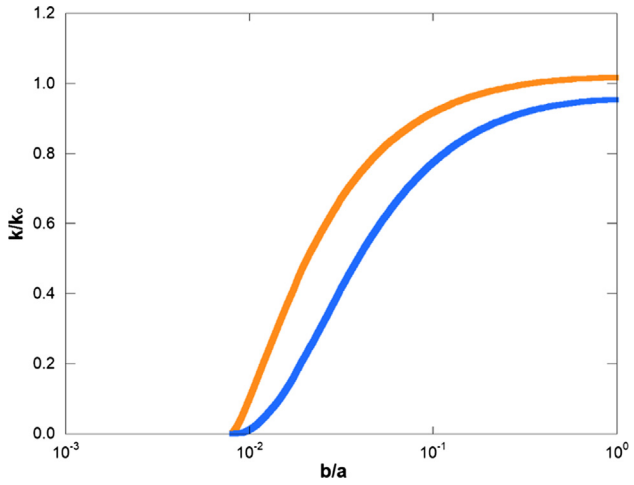

Fig. 3. Permeability evolution with changing aspect ratio. The cases shown are where the aspect ratio of pores is held constant under hydrostatic stress (blue) and where deformation only occurs along the minor semi-axis b (orange). (For interpretation of the references to color in this figure legend, the reader is referred to the web version of this article.)

3.2. Pore density

As stress is constant, the additional aperture closure at lower aspect ratios is due to strain becoming concentrated around the pore space. Fig. 4 shows the hypothetical distribution of strain for a shale as s/b varies, with db/u representing the change in aperture divided by the bulk deformation. The applied external stress is 10 MPa and the bulk stiffness is 1 GPa. Therefore, for all α's, the bulk strain is 10^{-2}. However, as α decreases the pore closure increases to the point where the entirety of the bulk deformation is accommodated in the pore space.

Having examined the theoretical basis for the influence of pore geometry and pore density on permeability evolution at constant stress, we now extend our results to a 2D model capturing the ensemble influence of these variables as well as the distribution of minerals around pores. We examine the cases of uniaxial compression and varying pore pressure.

4. Results and discussion

With anticipated results including changes in aperture Δb with varying strain, pore density, pore skeletal stiffness and pore pressure, we completed a simulation of bulk deformation on a series of 2D squares representing ellipsoid pores in rock. We formulated an analytical solution for changes in permeability with decreasing aspect ratio α which can extend the results in both configurations of the simulation. In the first configuration, we applied a uniaxial stress to the top face of each square and measured changes in aperture Δb while varying skeletal stiffness K_{sk}. We combine the results of the aspect ratio study to complete our set of variables, which for the first configuration are {ε, K_{sk}/K_m, s/b, α, k/k_0}. In the second configuration we held exterior boundaries at zero displacement and applied an increasing pore pressure from 0 to 100 MPa within the ellipsoid pore. We measured changes in aperture Δb while varying skeletal stiffness K_{sk}. We combine the results of the aspect ratio study to complete our set of variables, which for the second configuration are {P_p, K_{sk}/K_m, s/b, α, Δb/b}. Finally, we observe that the pore compression data and the pore dilation data represent competing processes in the subsurface and we locate regions where each variable exerts the dominant influence on net aperture response.

4.1. Uniaxial strain results

We convert changes in aperture Δb to permeability evolution k/k_0 for various combinations of the simulation variables in Figs. 5–7. For all plots showing k/k_0, k_0 is set at K_{sk}/K_m equal to unity such that aperture change is measured from a reference configuration that has no mismatch between material properties near the pore and the surrounding matrix. For k/k_0 values less than one, additional permeability is lost relative to the base case of K_{sk}/K_m equal to one. Similarly, for k/k_0 values greater than one, permeability is enhanced relative to the base case. In Fig. 5 we see that for a given strain, permeability remained almost constant when K_{sk} was much lower than K_m. As pores become stiffer than the surrounding matrix such that K_{sk}/K_m is greater than unity, strain becomes distributed further away from the pores and permeability increases relative to the base case. In this way, any given strain will cause a large permeability loss in the case of soft pores relative to the surrounding matrix or negligible permeability loss in the case of stiff pores relative to the surrounding matrix. Fig. 5 shows four different curves representing different pore spacing. As s/b increases, permeability evolution reaches a limit corresponding to maximum pore closure for the given strain. In these plots, strain is constant for all curves at $2e^{-3}$. The left-hand plot shows permeability evolution on semi-log axes while the right-hand plot is in log-log axes.

Fig. 6 shows aperture closure with varied K_{sk}/K_m at constant pore spacing—in this case, s/b is 100. As strain increases, the magnitude of

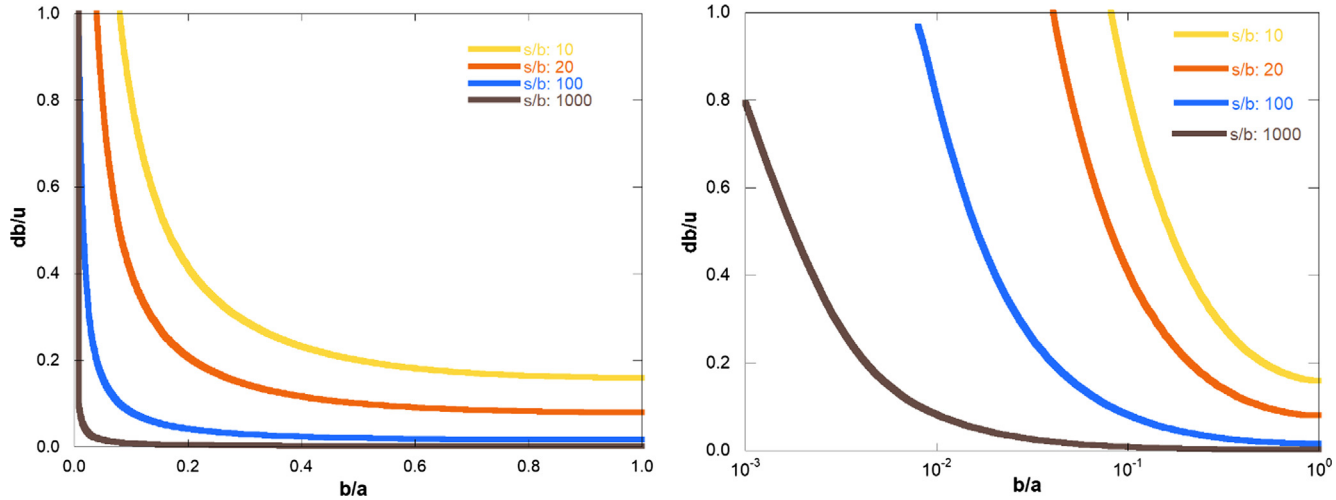

Fig. 4. db/u vs. α shows that as pores become more compliant, the bulk strain becomes concentrated in the pore space. The right-hand plot shows the same data on a log scale. As pore density increases, pores become less compliant.

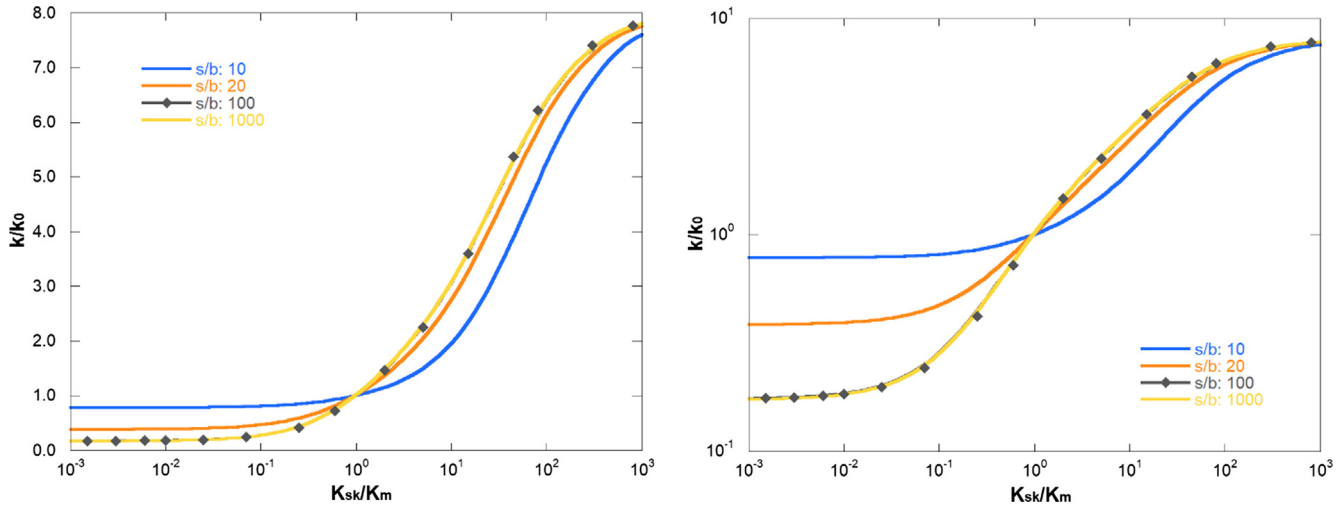

Fig. 5. Change in permeability k/k_0 vs. K_{sk}/K_m shows that as pore stiffness increases, aperture closure decreases. Bulk strain is 0.002 for all curves. The right-hand plot shows k/k_0 on a logarithmic scale.

aperture closure also increases. As in Fig. 5, when pores are soft compared to the surrounding matrix, aperture closure is almost constant for each strain. This is due to the pore closure being controlled by the matrix stiffness. Once the skeletal stiffness K_{sk} approaches K_m, it begins to exert a separate influence and Δb decreases. As each curve is at constant bulk strain, the decreasing nature of each curve as K_{sk} becomes much stiffer than K_m suggests that the strain becomes distributed in the matrix instead of around the pore itself. Fig. 6b shows permeability evolution with all curves normalized to k_0 at K_{sk}/K_m equal to unity. All curves collapse to one strain-independent curve, suggesting that at any strain the dependence of permeability evolution on the mineral distribution around the pore space is the same. The difference between the permeability evolution at a K_{sk}/K_m value of 10^{-1} and 10^{1} is more than an order of magnitude and could represent the difference between quartz cemented pores in a clay matrix and clay pores surrounded by a quartz matrix.

In Fig. 7 the change in aperture Δb/b is plotted with increasing external strain for different pore spacings. As additional strain is applied, a commensurate amount of pore closure occurs. As s/b increases, each pore becomes more compliant and more of the strain is distributed around the pore space up to an irreducible aperture closure limit where curves begin to overprint each other. As pore density increases such as the blue curve representing s/b equals 5, they become less compliant

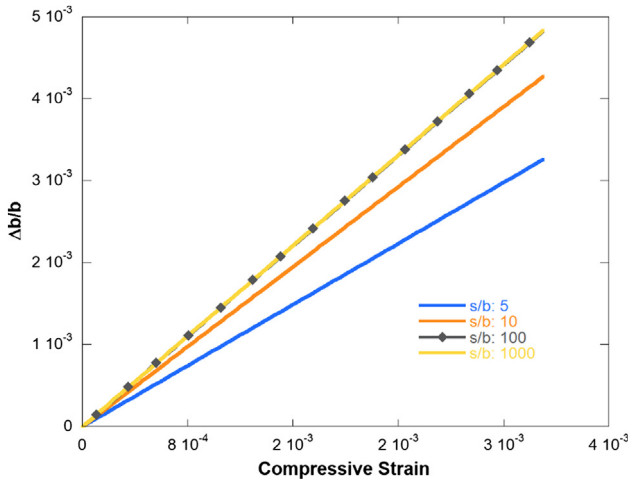

Fig. 7. Aperture closure with increasing external strain. As spacing between pores increases, aperture closure also increases.

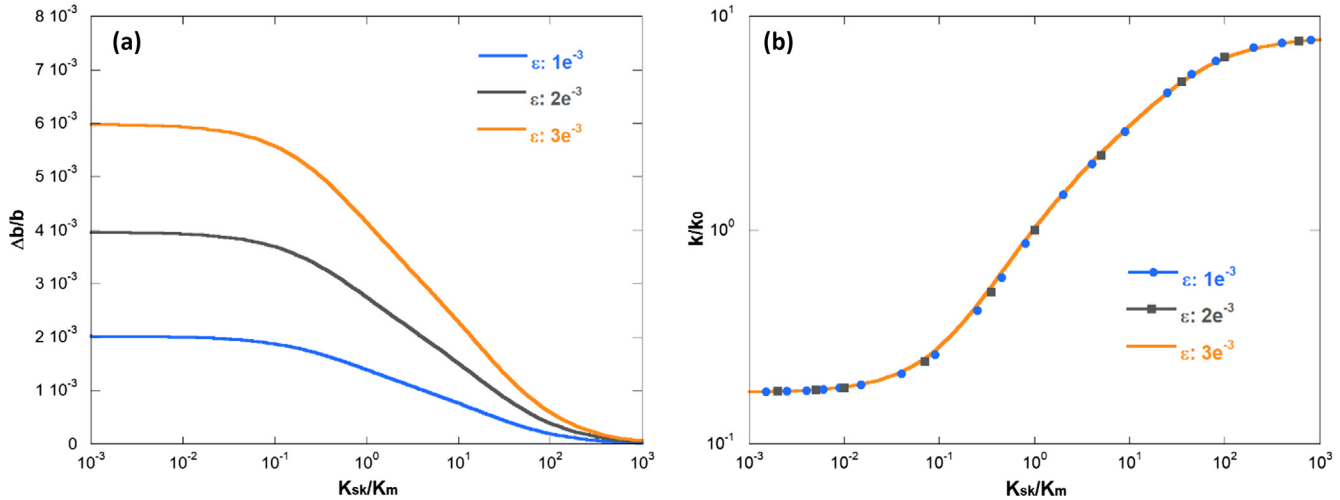

Fig. 6. Aperture closure with varying skeletal stiffness at constant pore spacing. Curves show iso-strains. (b) shows that when permeability evolution k/k_0 is normalized to K_{sk}/K_m of 1.0, all curves overprint each other and collapse to a single line.

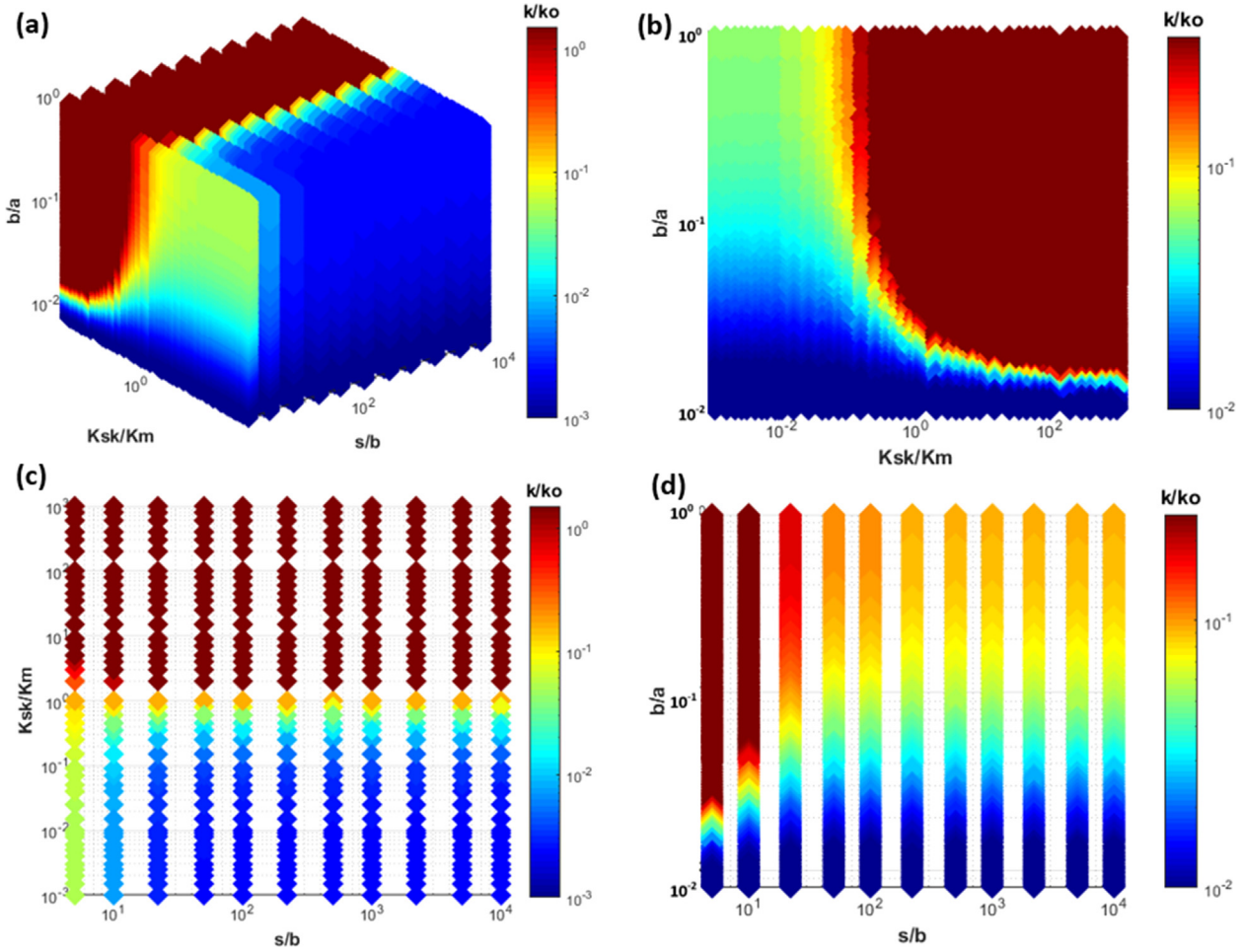

Fig. 8. Permeability evolution normalized to K_{sk}/K_m of 1.0 under uniaxial compression.

since the strain is distributed over more pores, resulting in less net closure for each pore.

4.2. Incorporating pore geometry

Results from Eq. (12) were integrated into the COMSOL simulation in order to observe the influence of all three variables in conjunction with each other. Fig. 8 shows all four combinations of the three variables with permeability evolution represented by color. In Fig. 8a, a 3D heat map of all three variables is shown with k/k_0 in color. Fig. 8a shows that for this configuration, spacing had the least effect on permeability while aspect ratio had the largest effect. As the aspect ratio approaches unity, pores compress less for a given strain than slit-like pores with lower aspect ratios. The aspect ratio is shown to be more important that the mineral distribution around the pore, as illustrated by variations in K_{sk}/K_m in Fig. 8b and c. Fig. 8b shows that while a soft pore made of clays or organics may experience additional closing, if the aspect ratio of the pore is greater than 0.10 much of the closure can be mitigated by the stiffer geometry. Fig. 8d shows that spacing may play in important role for shales as effective stress increases, such as in drilling and completions operations or pressure depletion.

To capture these effects, we expanded the simulation to include an additional analysis of spacing when pores are soft compared to the matrix. The above represents the case in which the pore stiffness is not much less than the surrounding matrix stiffness. If pore stiffness is much less than matrix stiffness, Δb is $s\varepsilon$ [28]. We expand the simulation by incorporating both s/b and strain in our 3D data. Using the cubic law (Eq. (8)) we find that as spacing increases, the permeability results should be modified by the below equation:

$$\frac{k_1}{k_0} = \left(1 - \frac{s\varepsilon_1}{b_0}\right)^3 \rightarrow \frac{k_1}{k_2} = \left(\frac{1 - \frac{s\varepsilon_1}{b_0}}{1 - \frac{s\varepsilon_2}{b_0}}\right)^3 \tag{13}$$

Results are plotted below in Fig. 9 for four different strains. It can be seen that as the strain increases, pore spacing becomes more important.

4.3. Varying pore pressure results

For the second configuration of the simulation, we held the exterior boundaries of a series of squares at zero displacement and varied the pore pressure within the ellipsoid pore. We varied the skeletal stiffness of the pore between 10^7 Pa and 10^{13} Pa while holding the matrix stiffness constant at 10^{10} Pa. Figs. 10–13 capture the main features of the aperture response to the pore pressure. In the case of the pore pressure study, positive Δb represents pore dilation and should be seen as a competing force to the external stress applied in the first part of the study. Both parts will be examined in tandem below, as the combination of the two reflects real world processes in the subsurface and in the lab.

Fig. 10 shows aperture dilation $\Delta b/b$ with evolving skeletal stiffness. For a given pore pressure, a rock will experience larger dilation with soft pores than with stiff pores. This suggests an additive competition in real world applications where pore pressure is being changed at the same time that an external stress is causing bulk strain. Notably, changing the s/b ratio does not produce significant differences as can be seen by the four curves overprinting each other. This differs from the uniaxial strain configuration where results scaled directly with each

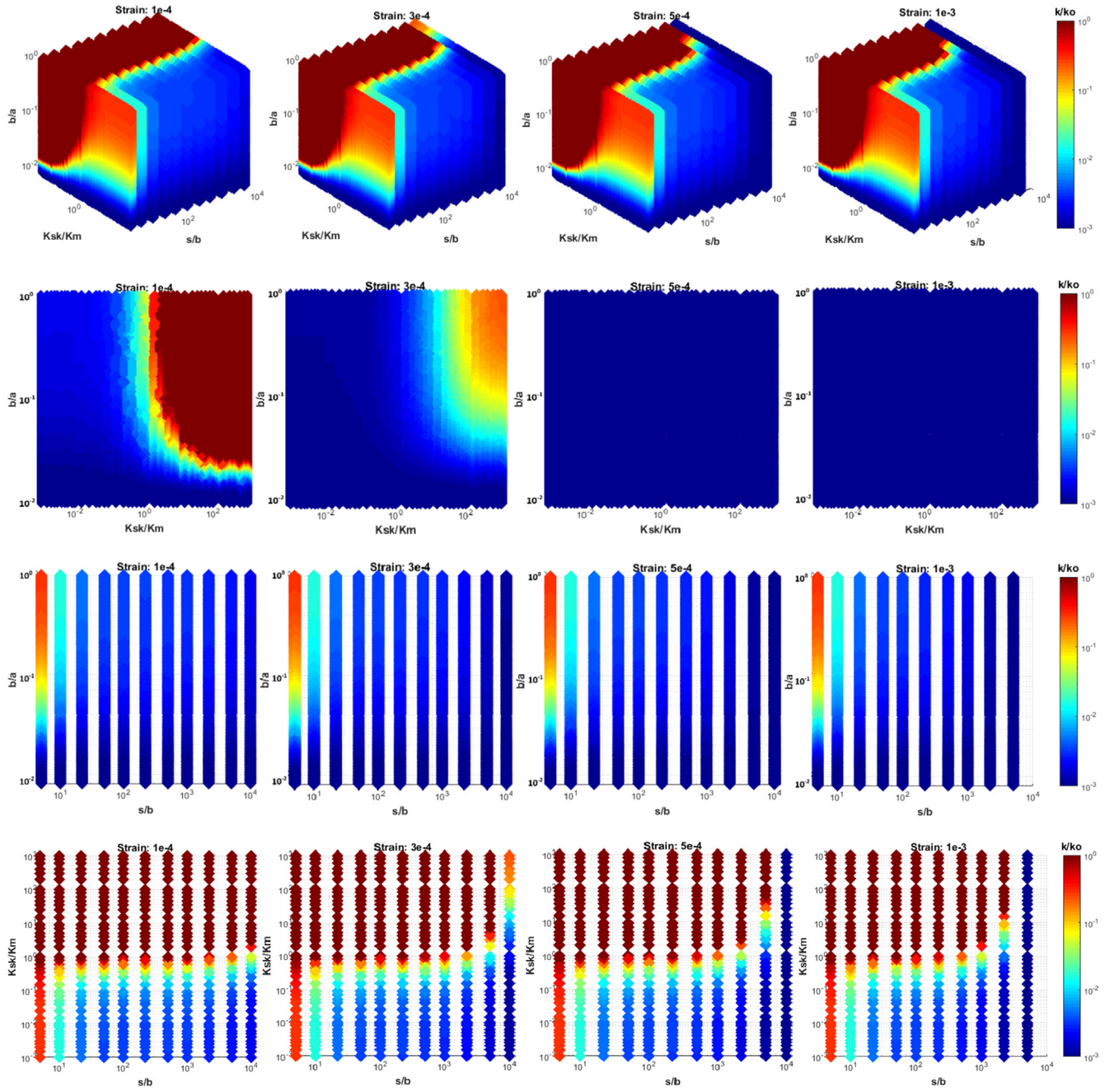

Fig. 9. Expanded simulation results to include the effect of spacing as strain increases.

magnitude of spacing.

There are several regions within Fig. 10. In the first region, from K_{sk}/K_m equals 10^{-3} to 10^{-1} all curves are overprinted at a linear slope that seems to be resumed in the third region where K_{sk}/K_m varies from 10^1 to 10^3. In the first region, $K_{sk} \ll K_m$, suggesting that aperture dilation is controlled by K_m. In the third region, $K_m \ll K_{sk}$, suggesting that aperture dilation is controlled by K_{sk}. In both regions, the stiffer material controlled the magnitude of aperture dilation Δb. There is a middle region where K_{sk}/K_m is between 10^{-1} and 10^1, such that material properties are relatively similar to each other. The inflection point is at K_{sk}/K_m equal to unity. In the first half of the middle region, where K_{sk}/K_m is between 10^{-1} and unity, the rate of aperture dilation begins to slow down as skeletal stiffness approaches the matrix stiffness. In the second half of the middle region, where K_{sk}/K_m is between unity and 10^1, the rate of aperture dilation slows down even more as the pore skeleton becomes increasingly stiffer.

Fig. 11 shows aperture dilation for different pore pressures with varying skeletal stiffness. For this plot, s/b is 100. As pore pressure increases, there is more dilation of the pore. While the pore pressure affects the dilation for a given K_{sk}/K_m, all pore pressures follow the same curve shape. Increasing pore pressure does not change the shape of the $\Delta b/b$ vs. K_{sk}/K_m curve, suggesting a linear relationship between pore pressure and pore dilation. This trend is confirmed in Fig. 12.

Fig. 12 shows aperture dilation with increasing pore pressure. Dilation appears to follow a linear trend with pore pressure. Three scenarios are shown: the left plot, middle, and right plots are K_{sk}/K_m equal to 10^{-2}, 10^0, and 10^2 respectively. Recalling Fig. 10, the middle plot shows the separation of the curves when both the skeletal stiffness and matrix stiffness are influencing the dilation. The left and right plots show Region 1 and 3 from Fig. 10, where spacing does not affect aperture dilation.

Fig. 13 shows increased aperture dilation with increasing pore

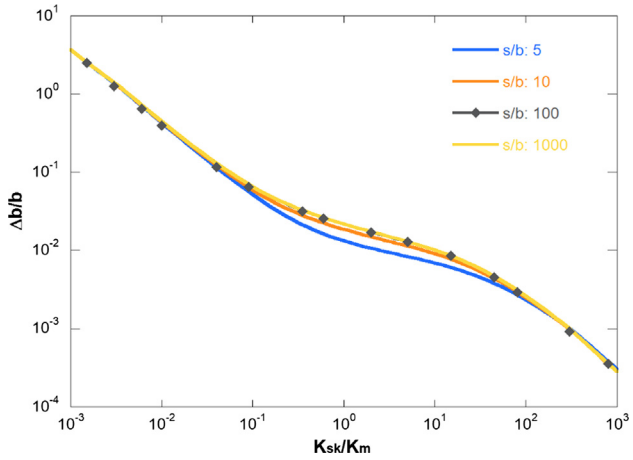

Fig. 10. Aperture dilation Δb/b with varying skeletal stiffness. All data are captured at a constant pore pressure of 60 MPa, and each curve represents a different pore density.

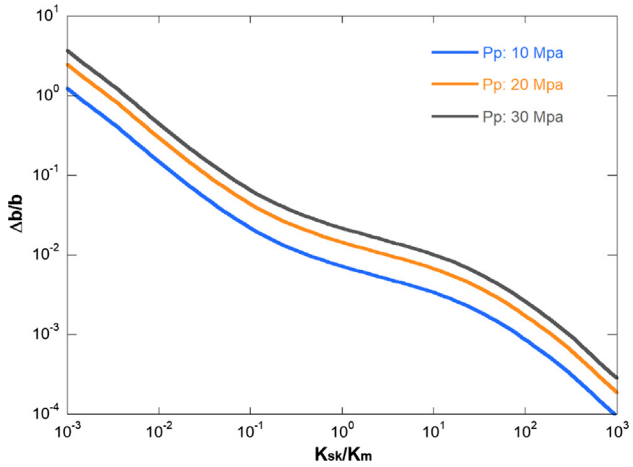

Fig. 11. Aperture dilation with varying K_{sk}/K_m for three different pore pressures.

pressure. Three curves are shown representing different K_{sk}/K_m ratios. As pores become softer, they experience larger dilation at the same pore pressure. This is the opposite of what was seen in the first configuration with uniaxial strain, suggesting that permeability loss experienced by soft pores may be mitigated by pressure management.

4.4. Incorporating pore geometry

We added Eq. (9) to the COMSOL data and plotted 3D heat maps of all three variables for the varying pore pressure configuration. Results

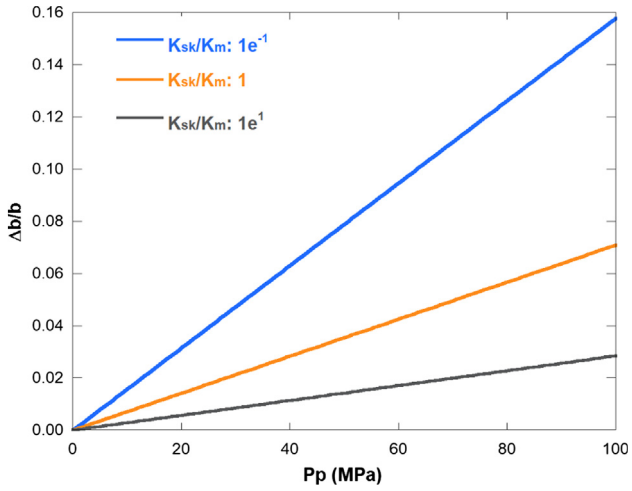

Fig. 13. Aperture dilation with increasing pore pressure for different skeletal stiffness ratios. The softest pore experienced the most dilation.

are shown below in Fig. 14. As can be seen below, the most notable feature of Fig. 14 is that in the case of varying pore pressure, the solution does not depend on pore spacing. This is different than the uniaxial stress configuration, in which increasing strain at high values of s/b reduced permeability. Physically, an increase in pore pressure should not be influenced by pore density because the deformation originates at the inside pore boundary whereas additional external stress causes a deformation that originates outside of the pore boundary. In the second case, the amount of material available for deformation—as determined by the spacing between pores—directly affects the amount of strain that must be accommodated by the pore space.

There are several factors that could affect the distribution of minerals around the pore space. Depositional environment determines the initial porosity and connectivity. In some rocks, dissolution, migration, and precipitation of calcite can create stiff pores encased in calcite surrounded by a clay matrix. Similarly, diagenesis of smectite will release dissolved silica that can lead to quartz cementation of pores [53,54].

The effect of spacing in the uniaxial stress simulation may be understated due to the way the model was constructed. In this study, two-dimensional squares with one non-interacting pore were considered. Since the existence of nearby pores are known to increase the compressibility of a rock [55,56], the ratio s/b necessarily influences a rock's compressibility.

The measured bulk modulus of a material is a weighted harmonic average of the bulk moduli of the individual mineral components. Therefore, rocks with identical mineralogy are expected to experience the same strain under a given stress. However, the distribution of the resulting strain will be directly related to the distribution of minerals

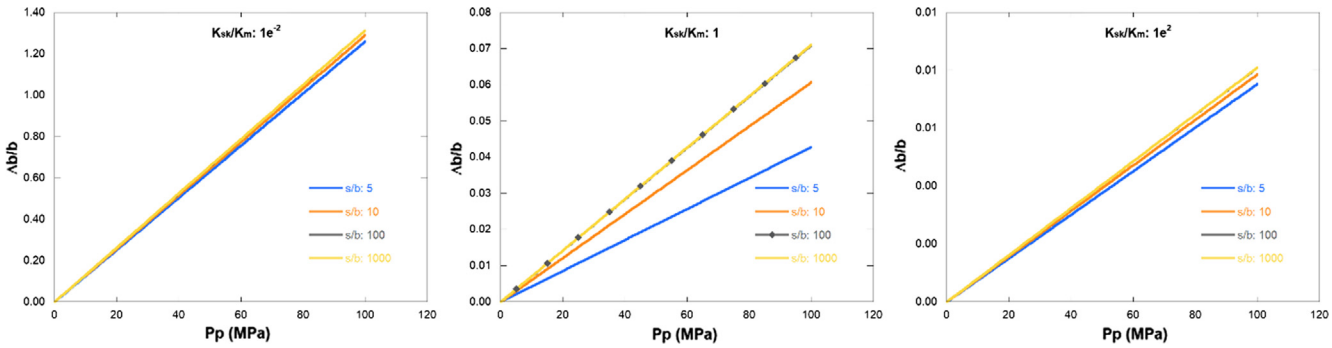

Fig. 12. Aperture dilation with varying pore pressure for different spacings.

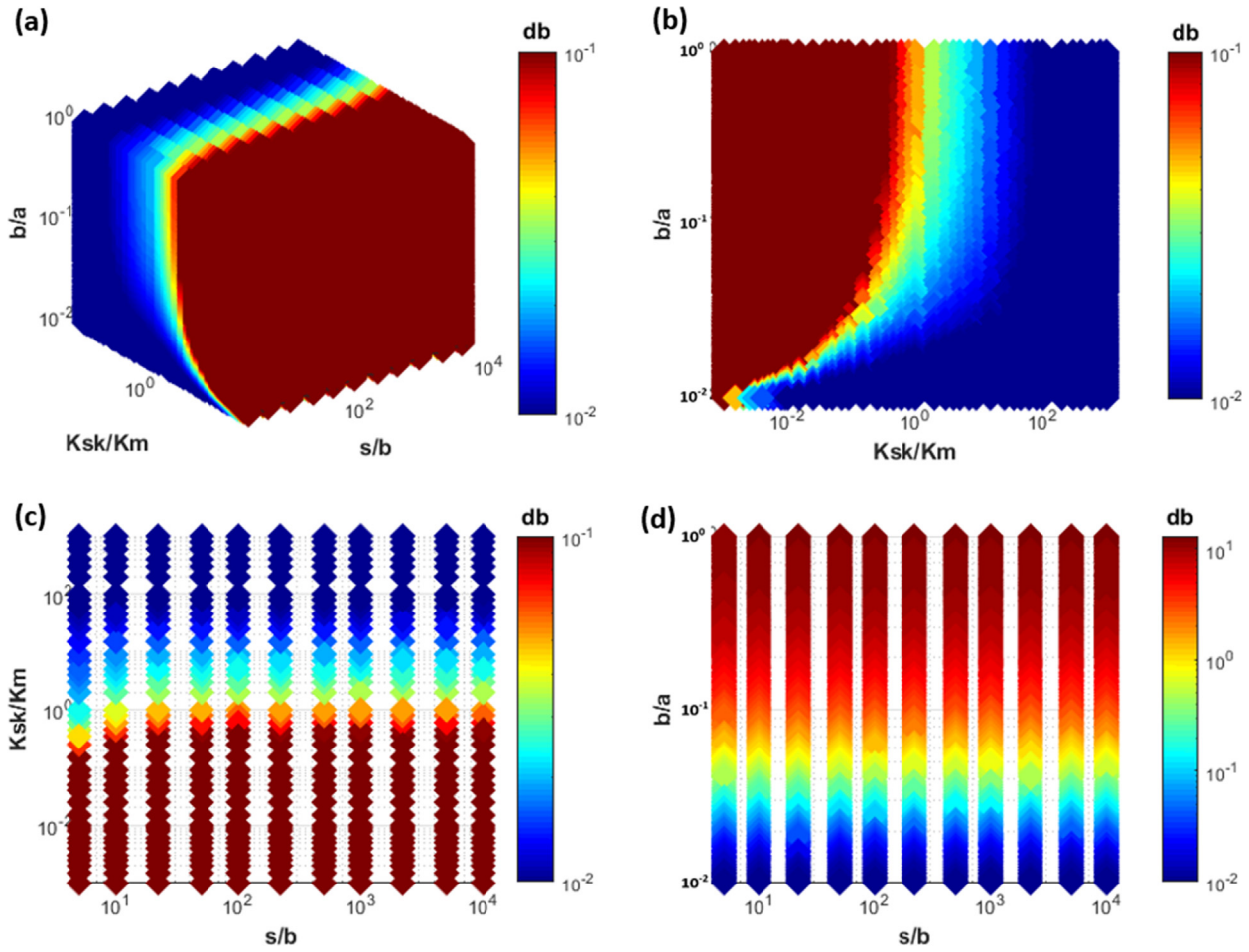

Fig. 14. Permeability evolution normalized to K_{sk}/K_m of 1.0 with changing pore pressure.

around the pores. In the Marcellus shale the porosity is believed to be concentrated in the clays and organics with stiffer components such as quartz and calcite being found in the far field region.

5. Summary and conclusion

We simulated the effects of mineral distribution around pores (K_{sk}/K_m), pore geometry (α), and pore spacing (s/b) on permeability evolution with changes in applied external stress and internal pore pressure. We found that the aspect ratio has the largest impact on both configurations. This is important for shales, as investigators report different aspect ratios for different basins. A basin like the Marcellus—consisting of slit-like pores with low aspect ratio—would see greater permeability reduction during pressure depletion than would a shale where the pores have larger aspect ratios. Marcellus shale has been shown to undergo significantly greater permeability reduction than Wolfcamp shale while undergoing identical deformation due to the influence of these three variables [52].

Changes in applied external stress and internal pore pressure are examples of different stress paths and may represent competing processes in the subsurface during production or injection operations. A common laboratory exercise is to measure permeability at increasing pore pressure while maintaining constant effective stress. While permeability should stay constant during such a stress path, this is not the typical outcome—some rocks undergo permeability enhancement while others undergo permeability reduction. The contributions of pore geometry, pore density, and mineral distribution around pores to this phenomenon should be the subject of further research.

The role of spacing was different for each configuration. In the case where the effective stress was changing because of an external stress, the role of spacing in permeability reduction became more pronounced as the spacing between pores increased. As spacing between pores increases, each pore must take more of the load of an external stress. As spacing between pores decreases, there are more pores available to accommodate a given stress and the strain is distributed such that each pore experiences less closure. Therefore, increased pore density makes pores less compliant. However, in the case of pore pressure variation, the results were independent of spacing.

Mineral distribution around the pore space showed that soft pores encased in a stiff matrix behave differently than stiff pores encased in a soft matrix. There are several distinct regions when plotting k/k_0 vs. K_{sk}/K_m. When K_{sk} is much lower than K_m, the change in permeability due to external strain is controlled by the pore stiffness. When K_{sk} is much higher than K_m, the change in permeability is controlled by the matrix stiffness. There is an inflection point where K_{sk} and K_m are equal. Between K_{sk}/K_m at 0.1 to 1, and again from 1 to 10, the behavior is more complex. This is the area of greatest interest as most natural systems would fall in this region.

An intriguing conclusion of this study is that the extreme heterogeneity typical of shale intervals will lead to a complex spatial response to changes in stress. Understanding how depositional history, thermal maturation, paleostress variations, and reservoir diagenesis contribute to the variables discussed in this analysis will allow for accurate vertical and lateral transport response modeling during subsurface operations.

The simulation shows that permeability evolution due to external strain is controlled by pore density, pore geometry, and pore stiffness; whereas permeability evolution due to pore pressure changes are controlled by pore geometry and pore stiffness alone. In some shales, the

magnitude of permeability evolution for a given external stress and internal pore pressure will be dominated by the permeability enhancement from pore pressure. In other shales—in particular shales where pore spacing is large—permeability controls may result in a net decrease. While pores in the bedding-parallel direction are generally aligned with each other, they may not be aligned along the direction of the principal stresses. Our study explored a uniaxial stress applied parallel to the semi-minor axis of the pore, but in the event of dipping beds this may not be the case. As overburden stress becomes more aligned with the semi-major axis of pores, we anticipate that our results would be observed to a lesser degree as the pore orientation relative to overburden stress would be stiffer. This work highlights the importance of understanding that no two shales are alike unless their aspect ratios, pore spacing, and mineral distribution around pores are all alike. As this is not generally the case, shales will respond differently to changes in stress brought about by drilling operations and pressure depletion. This suggests that pressure maintenance may be more important in shales with low aspect ratio, soft minerals around pores, and low pore density.

Acknowledgements

This work is a partial result of support from Chevron Energy Technology Company, and their support is gratefully acknowledged. We also thank three anonymous reviewers, whose recommendations significantly strengthened this manuscript.

References

[1] Ulm FJ, Abousleiman Y. The nanogranular nature of shale. Acta Geotech 2006;1(2):77–88.
[2] Horne SA. A statistical review of mudrock elastic anisotropy. Geophys Prospect 2013;61(4):817–26.
[3] Daigle H, Hayman NW, Kelly ED, Milliken KL, Jiang H. Fracture capture of organic pores in shales. Geophys Res Lett 2017;44(5):2167–76.
[4] Javadpour F, Fisher D, Unsworth M. Nanoscale gas flow in shale gas sediments. J Can Pet Technol 2007;46(10).
[5] Javadpour F. Nanopores and apparent permeability of gas flow in mudrocks (shales and siltstone). J Can Pet Technol 2009;48(08):16–21.
[6] Civan F, Rai CS, Sondergeld CH. Determining shale permeability to gas by simultaneous analysis of various pressure tests. SPE J 2012;17(03):717–26.
[7] Li X, Elsworth D. Geomechanics of CO2 enhanced shale gas recovery. J Nat Gas Sci Eng 2015;26:1607–19.
[8] Kumar H, Elsworth D, Mathews JP, Marone C. Permeability evolution in sorbing media: analogies between organic-rich shale and coal. Geofluids 2016;16(1):43–55.
[9] Costin LS. A microcrack model for the deformation and failure of brittle rock. J Geophys Res Solid Earth 1983;88(B11):9485–92.
[10] Loucks RG, Reed RM, Ruppel SC, Jarvie DM. Morphology, genesis, and distribution of nanometer-scale pores in siliceous mudstones of the Mississippian Barnett Shale. J Sediment Res 2009;79(12):848–61.
[11] Sondergeld CH, Newsham KE, Comisky JT, Rice MC, Rai CS. Petrophysical considerations in evaluating and producing shale gas resources. SPE unconventional gas conference. Society of Petroleum Engineers; 2010.
[12] Curtis ME, Sondergeld CH, Ambrose RJ, Rai CS. Microstructural investigation of gas shales in two and three dimensions using nanometer-scale resolution imaging Microstructure of Gas Shales. AAPG Bull 2012;96(4):665–77.
[13] Gu X, Mildner DFR. Ultra-small-angle neutron scattering with azimuthal asymmetry. J Appl Crystallogr 2016;49(3):934–43.
[14] Mavko G, Mukerji T, Dvorkin J. The rock physics handbook: tools for seismic analysis of porous media. Cambridge University Press; 2009.
[15] Bernabe Y, Brace WF, Evans B. Permeability, porosity and pore geometry of hot-pressed calcite. Mech Mater 1982;1(3):173–83.
[16] Sisavath S, Jing XD, Zimmerman RW. Effect of stress on the hydraulic conductivity of rock pores. Phys Chem Earth Part A 2000;25(2):163–8.
[17] Izadi G, Wang S, Elsworth D, Liu J, Wu Y, Pone D. Permeability evolution of fluid-infiltrated coal containing discrete fractures. Int J Coal Geol 2011;85(2):202–11.
[18] Budiansky B, O'connell RJ. Elastic moduli of a cracked solid. Int J Solids Struct 1976;12(2):81–97.
[19] Tsukrov I, Novak J. Effective elastic properties of solids with defects of irregular shapes. Int J Solids Struct 2002;39(6):1539–55.
[20] Sone H, Zoback MD. Mechanical properties of shale-gas reservoir rocks—Part 1: static and dynamic elastic properties and anisotropy. Geophysics 2013;78(5):D381–92.
[21] Bandyopadhyay K. Seismic anisotropy: geological causes and its implications to reservoir geophysics. Stanford University; 2009.
[22] Vernik L, Nur A. Ultrasonic velocity and anisotropy of hydrocarbon source rocks. Geophysics 1992;57(5):727–35.
[23] Zimmerman RW. Discussion: "the constitutive theory for fluid-filled porous materials. J Appl Mech 1985;52(4):983.
[24] Savin GN. Stress concentration around holes, (1961). English Translation. London: Pergamon Press; 1976.
[25] Zimmerman RW. Compressibility of two-dimensional cavities of various shapes. J Appl Mech 1986;53(3):500–4.
[26] Jasiuk I. Cavities vis-a-vis rigid inclusions: elastic moduli of materials with polygonal inclusions. Int J Solids Struct 1995;32(3–4):407–22.
[27] Walsh JB. The effect of cracks on the compressibility of rock. J Geophys Res 1965;70(2):381–9.
[28] Elsworth D. Thermal permeability enhancement of blocky rocks: one-dimensional flows No. 3-4 International journal of rock mechanics and mining sciences & geomechanics abstractsPergamon; 1989. p. 329–39.
[29] Goodman RE. Introduction to rock mechanics vol. 2. New York: Wiley; 1989.
[30] Ladeira FL, Price NJ. Relationship between fracture spacing and bed thickness. J Struct Geol 1981;3(2):179–83.
[31] Narr W, Suppe J. Joint spacing in sedimentary rocks. J Struct Geol 1991;13(9):1037–48.
[32] Chang CP, Angelier J, Huang CY. Subduction zone geodynamics. Berlin: Springer; 2009.
[33] Garrett KW, Bailey JE. Multiple transverse fracture in 90 cross-ply laminates of a glass fibre-reinforced polyester. J Mater Sci 1977;12(1):157–68.
[34] Narr W. Estimating average fracture spacing in subsurface rock. AAPG Bull 1996;80(10):1565–85.
[35] Ortega OJ, Marrett RA, Laubach SE. A scale-independent approach to fracture intensity and average spacing measurement. AAPG Bull 2006;90(2):193–208.
[36] Tsang YW, Witherspoon PA. Hydromechanical behavior of a deformable rock fracture subject to normal stress. J Geophys Res Solid Earth 1981;86(B10):9287–98.
[37] Brown SR. Fluid flow through rock joints: the effect of surface roughness. J Geophys Res Solid Earth 1987;92(B2):1337–47.
[38] Bonnelye A, Schubnel A, David C, Henry P, Guglielmi Y, Gout C, et al. Elastic wave velocity evolution of shales deformed under uppermost crustal conditions. J Geophys Res Solid Earth 2017;122(1):130–41.
[39] Bolton AJ, Maltman AJ, Fisher Q. Anisotropic permeability and bimodal pore-size distributions of fine-grained marine sediments. Mar Pet Geol 2000;17(6):657–72.
[40] Kwon O, Kronenberg AK, Gangi AF, Johnson B, Herbert BE. Permeability of illite-bearing shale: 1. Anisotropy and effects of clay content and loading. J Geophys Res Solid Earth 2004;109. (B10).
[41] Pan Z, Ma Y, Connell LD, Down DI, Camilleri M. Measuring anisotropic permeability using a cubic shale sample in a triaxial cell. J Nat Gas Sci Eng 2015;26:336–44.
[42] Huang S, Wu Y, Meng X, Liu L, Ji W. Recent advances on microscopic pore characteristics of low permeability sandstone reservoirs. Adv Geo-Energy Res 2018;2(2):122–34.
[43] Keller LM, Holzer L, Wepf R, Gasser P. 3D geometry and topology of pore pathways in Opalinus clay: implications for mass transport. Appl Clay Sci 2011;52(1–2):85–95.
[44] Chalmers GR, Bustin RM, Power IM. Characterization of gas shale pore systems by porosimetry, pycnometry, surface area, and field emission scanning electron microscopy/transmission electron microscopy image analyses: examples from the Barnett, Woodford, Haynesville, Marcellus, and Doig unitsCharacterization of Gas Shale Pore Systems. AAPG Bull 2012;96(6):1099–119.
[45] Ross DJ, Bustin RM. The importance of shale composition and pore structure upon gas storage potential of shale gas reservoirs. Mar Pet Geol 2009;26(6):916–27.
[46] Ausbrooks R, Hurley NF, May A, Neese DG. Pore-size distributions in vuggy carbonates from core images, NMR, and capillary pressure. Society of Petroleum Engineers; 1999.
[47] Yao Y, Liu D, Che Y, Tang D, Tang S, Huang W. Petrophysical characterization of coals by low-field nuclear magnetic resonance (NMR). Fuel 2010;89(7):1371–80.
[48] Meng M, Ge H, Ji W, Wang X. Research on the auto-removal mechanism of shale aqueous phase trapping using low field nuclear magnetic resonance technique. J Petrol Sci Eng 2016;137:63–73.
[49] Yang Y, Zhang W, Gao Y, Wan Y, Su Y, An S, et al. Influence of stress sensitivity on microscopic pore structure and fluid flow in porous media. J Nat Gas Sci Eng 2016;36:20–31.
[50] An S, Yao J, Yang Y, Zhang L, Zhao J, Gao Y. Influence of pore structure parameters on flow characteristics based on a digital rock and the pore network model. J Nat Gas Sci Eng 2016;31:156–63.
[51] Chen X, Zhou Y. Applications of digital core analysis and hydraulic flow units in petrophysical characterization. Adv Geo-Energy Res 2017;1(1):18–30.
[52] Schwartz B, Huffman K, Thornton D, Elsworth D. A strain based approach to calculate disparities in pore structure between shale basins during permeability evolution. J Nat Gas Sci Eng 2019;68:102893.
[53] Berger G, Lacharpagne JC, Velde B, Beaufort D, Lanson B. Kinetic constraints on illitization reactions and the effects of organic diagenesis in sandstone/shale sequences. Appl Geochem 1997;12(1):23–35.
[54] Metz V, Amram K, Ganor J. Stoichiometry of smectite dissolution reaction. Geochim Cosmochim Acta 2005;69(7):1755–72.
[55] Fond C, Riccardi A, Schirrer R, Montheillet F. Mechanical interaction between spherical inhomogeneities: an assessment of a method based on the equivalent inclusion. Eur J Mech Series A Solids 2001;20(1):59–76.
[56] Chalon F, Montheillet F. The interaction of two spherical gas bubbles in an infinite elastic solid. J Appl Mech 2003;70(6):789–98.